Available online at www.sciencedirect.com
ScienceDirect
Journal of Computational Physics 225 (2007) 33–50
JOURNAL OF COMPUTATIONAL PHYSICS
www.elsevier.com/locate/jcp

Application of the symplectic finite-difference time-domain scheme to electromagnetic simulation

Wei Sha *, Zhixiang Huang, Xianliang Wu, Mingsheng Chen

Key Laboratory of Intelligent Computing & Signal Processing, Anhui University, Hefei 230039, China

Received 2 March 2006; received in revised form 13 November 2006; accepted 13 November 2006
Available online 17 January 2007

Abstract

An explicit fourth-order finite-difference time-domain (FDTD) scheme using the symplectic integrator is applied to electromagnetic simulation. A feasible numerical implementation of the symplectic FDTD (SFDTD) scheme is specified. In particular, new strategies for the air–dielectric interface treatment and the near-to-far-field (NFF) transformation are presented. By using the SFDTD scheme, both the radiation and the scattering of three-dimensional objects are computed. Furthermore, the energy-conserving characteristic hold for the SFDTD scheme is verified under long-term simulation. Numerical results suggest that the SFDTD scheme is more efficient than the traditional FDTD method and other high-order methods, and can save computational resources.

Keywords: Symplectic integrator; High-order difference; Long-term simulation; Energy conservation; Radiation and scattering

1. Introduction

As the most standard algorithm, the traditional finite-difference time-domain (FDTD) method [1,2], which is explicit second-order-accurate in both space and time, has been widely applied to electromagnetic computation and simulation. The main advantages of the FDTD-based techniques for solving electromagnetic problems are computational simplicity and low operation count. Furthermore, it is very well suited to analyze transient problems and is very good at modeling inhomogeneous geometries. Most important of all, the method can readily be implemented on the massive computers.

However, the FDTD method has two primary drawbacks, one is the inability to accurately model curved complex surfaces and material discontinuity by using the staircasing approach with structured grids, and another is the significant accumulated errors from numerical instability, dispersion and anisotropy. Hence fine grids must be required to obtain satisfying numerical results, which leads to vast memory

* Corresponding author. Tel.: +86 551 510 6294.
E-mail address: ws108@ahu.edu.cn (W. Sha).

0021-9991/$ - see front matter © 2006 Elsevier Inc. All rights reserved.
doi:10.1016/j.jcp.2006.11.027

requirements and high computational costs, especially for electrically large domains and for long-term simulation.

For the first pitfall, a variety of alternative methods in conjunction with unstructured grids are proposed to reduce the inaccuracy owing to the staircase approximation, including finite-volume time-domain (FVTD) [3–5], finite-element time-domain (FETD) [6–8], and discontinuous Galerkin time-domain (DGTD) methods [9–11]. First of all, in the FVTD method, the Maxwell's equations are written in the conservative form. The fields, located generally at the center of a cell, are evaluated as the sum of fluxes taken at the faces of the cell. Yet, the method fails in being at the same time, stable, nondissipative and easily extendible to high-order accuracy. Secondly, the FETD approach expresses the Maxwell's equations by a variational formulation. Although the generated nondiagonal mass-matrices have been accelerated by using the accurate mass lumping technique, application of the technique to high-order approximation is still not obvious. Thirdly, the DGTD method uses piecewise high-order polynomials on quadrilateral or triangular elements for spatial discretization of the Maxwell's equations and uses implicit Runge–Kutta (R–K) or explicit leap-frog method for time integration. It can achieve high-order accuracy and can be easy to handle complex geometries. However, the DGTD is based on the FE type mesh, more storage and number of floating point operations per mesh point are required. Besides, high-order symplectic scheme for temporal discretization is an ongoing work.

To overcome the second problem, other high-order spatial discretization strategies have been put forward. For example, based on orthonormal wavelet expansions, a multiresolution time-domain (MRTD) method [12] was advanced. Yet, the method is difficult to handle material interface for modeling the three-dimensional complex objects. Another approach is the staggered fourth-order FDTD method [13,14], which retains the simplicity of the original Yet algorithm and can save computational resources with coarse grids compared to the traditional FDTD method. However, the approach must set lower Courant–Friedrichs–Levy (CFL) number to comply with the stability criterion.

In sum, the developed spatial discretization methods above are not enough for optimum electromagnetic simulation, for one reason that the implicit R–K method implemented in the temporal direction to some extent destroys the symplectic structure of the electromagnetic system, and for another reason that the nondissipative leapfrog algorithm for time integration only has second-order accuracy. Hence developing energy-preserving high-order time-schemes for matching high-order space-schemes is necessary. The symplectic schemes [15–20] include a variety of different temporal discretization strategies designed to preserve the global symplectic structure of the phase space for a Hamiltonian system. They have demonstrated their advantages in numerical computation for the Hamiltonian system, especially under long-term simulation. Since Maxwell's equations can be written as an infinite dimensional Hamiltonian system, a stable and accurate solution can be obtained by using the symplectic schemes, which preserve the energy of the Hamiltonian system constant.

As a numerical integration scheme, the symplectic integrator [21–23] and multi-symplectic integrator [24–27] have been introduced to the computational electromagnetism. Recently, a direct symplectic integrator [28,29] employed to analyze the waveguide's eigenmode has been successfully realized by Hirono, and the symplectic finite-difference time-domain (SFDTD) scheme is nondissipative and saves memory. Then the improved exponential operator coefficients [30] optimize the symplectic integrator. Moreover, the total field and scattered field technique [31,32] further promotes the practical utilization of the scheme to the three-dimensional electromagnetic simulation.

In this paper, the SFDTD scheme is used to solve the electromagnetic radiation, penetration and scattering problems. To efficiently implement the scheme, required and feasible equations are derived. In particular, new strategies for the air–dielectric interface treatment and the near-to-far-field (NFF) transformation are proposed. By using the SFDTD scheme, the propagation of one-dimensional Gaussian pulse, the radiation of three-dimensional vertical electric dipole, and the scattering of three-dimensional perfectly conducting cube and dielectric sphere are simulated.

The paper is organized as follows. The general formulations of the SFDTD scheme, the air–dielectric interface treatment, the perfectly matched layer (PML) absorbing boundary condition (ABC), the total field and scattered field (TF–SF) technique, and the NFF transformation are specified in Section 2. The comparisons to other methods are analyzed in Section 3, followed by the numerical results presented in Section 4. Finally, summary is concluded in Section 5.

2. Theory

2.1. General formulations

A function of space and time evaluated at a discrete point in the Cartesian lattice and at a discrete stage in the time step can be notated as

$$F(x,y,z,t) = F^{n+l/m}(i\Delta_x, j\Delta_y, k\Delta_z, (n+\tau_l)\Delta_t), \tag{1}$$

where Δ_x, Δ_y, and Δ_z are, respectively, the lattice space increments in the x, y, and z coordinate directions, Δ_t is the time increment, i, j, k, n, l, and m are integers, $n + l/m$ denotes the lth stage after n time steps, m is the total stage number, and τ_l is the fixed time with respect to the lth stage.

For the spatial direction, the explicit fourth-order-accurate difference expressions in conjugation with the staggered Yee lattice are used to discretize the first-order spatial derivatives, as follows:

$$\left(\frac{\partial F^{n+l/m}}{\partial \delta}\right)_h = \frac{9}{8}\times\frac{F^{n+l/m}(h+1/2) - F^{n+l/m}(h-1/2)}{\Delta_\delta} + \frac{-1}{8}\times\frac{F^{n+l/m}(h+3/2) - F^{n+l/m}(h-3/2)}{3\Delta_\delta} + O(\Delta_\delta^4), \tag{2}$$

where $\delta = x, y, z$ and $h = i, j, k$.

For the temporal direction, a helicity Hamiltonian [33] for the Maxwell's equations in homogeneous, lossless, and sourceless medium is introduced as

$$G(\mathbf{H},\mathbf{E}) = \frac{1}{2}\left(\frac{1}{\varepsilon}\mathbf{H}\cdot\nabla\times\mathbf{H} + \frac{1}{\mu}\mathbf{E}\cdot\nabla\times\mathbf{E}\right), \tag{3}$$

where $\mathbf{E} = (E_x, E_y, E_z)^{\mathrm{T}}$ is the electric field vector, $\mathbf{H} = (H_x, H_y, H_z)^{\mathrm{T}}$ is the magnetic field vector, and ε and μ are the permittivity and permeability of the medium.

Symplectic integrator can be generated starting from the canonical Euler–Hamilton equations of the form

$$\frac{\partial \mathbf{H}}{\partial t} = -\frac{\partial G}{\partial \mathbf{E}}, \quad \frac{\partial \mathbf{E}}{\partial t} = \frac{\partial G}{\partial \mathbf{H}}. \tag{4}$$

According to the variational principle, (4) can be rewritten as

$$\frac{\partial}{\partial t}\begin{pmatrix}\mathbf{H}\\ \mathbf{E}\end{pmatrix} = (U+V)\begin{pmatrix}\mathbf{H}\\ \mathbf{E}\end{pmatrix}, \tag{5}$$

$$U = \begin{pmatrix}\{0\}_{3\times3} & -\mu^{-1}R\\ \{0\}_{3\times3} & \{0\}_{3\times3}\end{pmatrix}, \quad V = \begin{pmatrix}\{0\}_{3\times3} & \{0\}_{3\times3}\\ \varepsilon^{-1}R & \{0\}_{3\times3}\end{pmatrix}, \tag{6}$$

$$R = \begin{pmatrix}0 & -\frac{\partial}{\partial z} & \frac{\partial}{\partial y}\\ \frac{\partial}{\partial z} & 0 & -\frac{\partial}{\partial x}\\ -\frac{\partial}{\partial y} & \frac{\partial}{\partial x} & 0\end{pmatrix}, \tag{7}$$

where $\{0\}_{3\times3}$ is the 3×3 null matrix, and R is the 3×3 matrix representing the three-dimensional curl operator.

Using the product of elementary symplectic mapping, the exact solution of (5) from $t = 0$ to $t = \Delta_t$ can be approximately constructed [16]

$$\exp(\Delta_t(U+V)) = \prod_{l=1}^{m}\exp(d_l\Delta_t V)\exp(c_l\Delta_t U) + O(\Delta_t^{p+1}), \tag{8}$$

where c_l and d_l are the constant coefficients of the symplectic integrator, and p is the order of the approximation. Here we use $m = 5$ and $p = 4$, a five-stage fourth-order symplectic integrator is obtained. The coefficients can be found by using the Baker–Campbell–Hausdorff (BCH) formula [16,17,20].

In order to get the simplified SFDTD formulations, the scaled electric field vector $\hat{\mathbf{E}}$ is defined by the following change-of-variable formula:

$$\hat{\mathbf{E}} = \sqrt{\frac{\varepsilon_0}{\mu_0}}\mathbf{E}, \tag{9}$$

where ε_0 and μ_0 are the permittivity and permeability of free space.

The SFDTD scheme, which is explicit fourth-order accurate in both space and time, can be obtained by the discretization approaches above. The detailed expression of the x component of the scaled electric field $\hat{\mathbf{E}}$ at the lth stage can be written as

$$\begin{aligned}\hat{E}_x^{n+l/m}\left(i+\frac{1}{2},j,k\right) = {} & \hat{E}_x^{n+(l-1)/m}\left(i+\frac{1}{2},j,k\right) + \frac{1}{\bar{\varepsilon}_{\mathrm{r}}\left(i+\frac{1}{2},j,k\right)} \\ & \times \left\{ \alpha_{y1} \times \left[H_z^{n+l/m}\left(i+\frac{1}{2},j+\frac{1}{2},k\right) - H_z^{n+l/m}\left(i+\frac{1}{2},j-\frac{1}{2},k\right)\right] \right. \\ & - \alpha_{z1} \times \left[H_y^{n+l/m}\left(i+\frac{1}{2},j,k+\frac{1}{2}\right) - H_y^{n+l/m}\left(i+\frac{1}{2},j,k-\frac{1}{2}\right)\right] \\ & + \alpha_{y2} \times \left[H_z^{n+l/m}\left(i+\frac{1}{2},j+\frac{3}{2},k\right) - H_z^{n+l/m}\left(i+\frac{1}{2},j-\frac{3}{2},k\right)\right] \\ & \left. -\alpha_{z2} \times \left[H_y^{n+l/m}\left(i+\frac{1}{2},j,k+\frac{3}{2}\right) - H_y^{n+l/m}\left(i+\frac{1}{2},j,k-\frac{3}{2}\right)\right]\right\},\end{aligned} \tag{10}$$

$$\alpha_{y1} = \frac{9}{8}d_l \times \mathrm{CFL}_y, \quad \alpha_{z1} = \frac{9}{8}d_l \times \mathrm{CFL}_z, \tag{11}$$

$$\alpha_{y2} = \frac{-1}{24}d_l \times \mathrm{CFL}_y, \quad \alpha_{z2} = \frac{-1}{24}d_l \times \mathrm{CFL}_z, \tag{12}$$

$$\mathrm{CFL}_y = \frac{1}{\sqrt{\mu_0\varepsilon_0}}\frac{\Delta_t}{\Delta_y}, \quad \mathrm{CFL}_z = \frac{1}{\sqrt{\mu_0\varepsilon_0}}\frac{\Delta_t}{\Delta_z}, \tag{13}$$

where $\bar{\varepsilon}_{\mathrm{r}}$ denotes the averaged relative permittivity at point $(i+\frac{1}{2},j,k)$. For the cubic lattice case, $\Delta_x = \Delta_y = \Delta_z = \Delta_\delta$ and $\mathrm{CFL}_x = \mathrm{CFL}_y = \mathrm{CFL}_z = \mathrm{CFL}_\delta$. The uniform constant CFL_δ is called the CFL number.

Compared with the Hirono's scheme using four different averaged permittivities in Ref. [29], our scheme using the only averaged permittivity can save considerable memory. With the help of our scheme, the computational complexity of Eq. (10) is reduced from O(8) to O(5) in every stage.

2.2. Air–dielectric interface treatment

Many efforts to deal with the air–dielectric interface for high-order difference have been made [34–38]. The common idea on the problem is to derive the one-sided difference operators, moreover, the instability can be partially solved by introducing dissipative time integration [34] or filtering approach [35]. However, accurate and efficient numerical experiments relative to the three-dimensional scattering problems have not been verified. Here we propose another applicable strategy to solve the problem, which not only can achieve accurate results, but also places little additional computation on the original SFDTD scheme.

The integral form of the Ampere's law can be defined as (14) and the general Ampere's contours are drawn in Fig. 1

$$\frac{\partial}{\partial t}\int\int_S \varepsilon_{\mathrm{r}}\hat{\mathbf{E}}\cdot \mathrm{d}\boldsymbol{S} = \frac{1}{\sqrt{\mu_0\varepsilon_0}}\oint_C \mathbf{H}\cdot \mathrm{d}\boldsymbol{L}, \tag{14}$$

where ε_{r} are the local relative permittivities over the patch S, S can be patch S_1 (dark gray) or patch S_2 (both light gray and dark gray), and C can be contour C_1 (one arrow) or contour C_2 (double arrows).

The treatment of material discontinuity is based on the following assumption:

(1) Magnetic field value at the midpoint of one side of the contour equals the averaged value of the magnetic field component along the side.

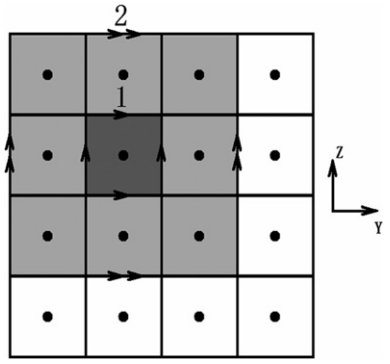

Fig. 1. The general Ampere's contours for the SFDTD scheme, where the dots denote $\hat{E}_x$, the horizontal arrows denote H_y, and the vertical arrows denote H_z.

(2) Electric field value in the center of the contour equals the averaged value of the electric field component over the corresponding patch.
(3) Permittivity in the center of the contour equals the averaged permittivity over the corresponding patch.

Applying the Ampere's law to both the contour C_1 and the contour C_2, the formulation (14) can be converted to

$$\begin{aligned}
&\frac{1}{A_{S_1}}\int\int_{S_1}\varepsilon_{\mathrm{r}}\,\mathrm{d}S_1\times\left[\hat{E}_x^{n+l/m}\left(i+\frac{1}{2},j,k\right)-\hat{E}_x^{n+(l-1)/m}\left(i+\frac{1}{2},j,k\right)\right]\\
&\quad=d_l\times\left\{\mathrm{CFL}_y\times\left[H_z^{n+l/m}\left(i+\frac{1}{2},j+\frac{1}{2},k\right)-H_z^{n+l/m}\left(i+\frac{1}{2},j-\frac{1}{2},k\right)\right]\right.\\
&\quad\left.-\mathrm{CFL}_z\times\left[H_y^{n+l/m}\left(i+\frac{1}{2},j,k+\frac{1}{2}\right)-H_y^{n+l/m}\left(i+\frac{1}{2},j,k-\frac{1}{2}\right)\right]\right\},
\end{aligned}\tag{15}$$

$$\begin{aligned}
&\frac{1}{A_{S_2}}\int\int_{S_2}\varepsilon_{\mathrm{r}}\,\mathrm{d}S_2\times\left[\hat{E}_x^{n+l/m}\left(i+\frac{1}{2},j,k\right)-\hat{E}_x^{n+(l-1)/m}\left(i+\frac{1}{2},j,k\right)\right]\\
&\quad=\frac{1}{3}d_l\times\left\{\mathrm{CFL}_y\times\left[H_z^{n+l/m}\left(i+\frac{1}{2},j+\frac{3}{2},k\right)-H_z^{n+l/m}\left(i+\frac{1}{2},j-\frac{3}{2},k\right)\right]\right.\\
&\quad\left.-\mathrm{CFL}_z\times\left[H_y^{n+l/m}\left(i+\frac{1}{2},j,k+\frac{3}{2}\right)-H_y^{n+l/m}\left(i+\frac{1}{2},j,k-\frac{3}{2}\right)\right]\right\},
\end{aligned}\tag{16}$$

where A_{S_1} and A_{S_2} are, respectively, the area of S_1 and the area of S_2.

In view of the fact that the integral form of the Maxwell's equations is identical to the differential form of the Maxwell's equations, we adopt weighting method for the integral equations (15) and (16) to derive the discretized differential equation (10). By adding (15) multiplied by 9/8 to (16) multiplied by $-1/8$, the averaged relative permittivity $\bar{\varepsilon}_{\mathrm{r}}$ in (10) can be expressed as

$$\bar{\varepsilon}_{\mathrm{r}}=\frac{9}{8A_{S_1}}\int\int_{S_1}\varepsilon_r\,\mathrm{d}S_1-\frac{1}{8A_{S_2}}\int\int_{S_2}\varepsilon_{\mathrm{r}}\,\mathrm{d}S_2.\tag{17}$$

Using little CPU time, the integral can be computed at the initial process by refined subcell modeling. In addition, the averaged conductivity can be treated in the same way.

2.3. Perfectly matched layer absorbing boundary condition

The PML technique [39–41] is very efficient for absorbing electromagnetic wave and solving the unbounded problems. The formulation of each subcomponent in the PML region can be deduced, if the basic

formulations, such as (10), are extended for the lossy medium and each field component is split into two subcomponents. The discretized z subcomponent of the $\hat{E}_x$ field in the PML region can be deduced as

$$\hat{E}_{xz}^{n+l/m}\left(i+\frac{1}{2},j,k\right)=\exp\left(-d_l\frac{\Delta_t\sigma_z\left(i+\frac{1}{2},j,k\right)}{\varepsilon_0}\right)\times\hat{E}_{xz}^{n+(l-1)/m}\left(i+\frac{1}{2},j,k\right)+\frac{1-\exp\left(-d_l\frac{\Delta_t\sigma_z\left(i+\frac{1}{2},j,k\right)}{\varepsilon_0}\right)}{d_l\frac{\Delta_t\sigma_z\left(i+\frac{1}{2},j,k\right)}{\varepsilon_0}}\times\left\{-\alpha_{z1}\times\left[H_y^{n+l/m}\left(i+\frac{1}{2},j,k+\frac{1}{2}\right)-H_y^{n+l/m}\left(i+\frac{1}{2},j,k-\frac{1}{2}\right)\right]-\alpha_{z2}\times\left[H_y^{n+l/m}\left(i+\frac{1}{2},j,k+\frac{3}{2}\right)-H_y^{n+l/m}\left(i+\frac{1}{2},j,k-\frac{3}{2}\right)\right]\right\},\tag{18}$$

where σ_z is the local electric conductivity at $(i+\frac{1}{2},j,k)$ in the PML region. Polynomial conductivities are employed varying from zeros at the vacuum-layer interface to σ_{zm} at the outer side of PML layer, i.e.

$$\sigma_z(\rho)=\sigma_{zm}\left(\frac{\rho}{\chi}\right)^{\beta},\tag{19}$$

where χ is the layer thickness, ρ is the distance from the interface, and β is the polynomial order.

2.4. Total field and scattered field technique

Without loss of generality, it can be assumed that an incident plane wave propagates along the z direction and the electric field is polarized along the x direction. The relative topic about the TF–SF technique for the SFDTD scheme can be found in [31,32].

2.4.1. One-dimensional incident field

The incident electric field $\hat{E}_{x,\mathrm{inc}}$ is added at a source point k_s and the one-dimensional equation in free space can be written as

$$\hat{E}_{x,\mathrm{inc}}^{n+l/m}(k)=\hat{E}_{x,\mathrm{inc}}^{n+(l-1)/m}(k)-\alpha_{z1}\times\left[H_{y,\mathrm{inc}}^{n+l/m}\left(k+\frac{1}{2}\right)-H_{y,\mathrm{inc}}^{n+l/m}\left(k-\frac{1}{2}\right)\right]-\alpha_{z2}\times\left[H_{y,\mathrm{inc}}^{n+l/m}\left(k+\frac{3}{2}\right)-H_{y,\mathrm{inc}}^{n+l/m}\left(k-\frac{3}{2}\right)\right],\tag{20}$$

$$\hat{E}_{x,\mathrm{inc}}^{n+l/m}(k_\mathrm{s})=\Psi^{n+l/m}((n+\tau_l)\Delta_t),\quad \tau_l=\sum_{r=1}^{l}c_\mathrm{r},\tag{21}$$

where $H_{y,\mathrm{inc}}$ is the incident magnetic field, Ψ is a function of time, and the c_r has been defined in (8).

Likewise, the one-dimensional PML ABC can be derived through (18).

2.4.2. Three-dimensional source conditions

The source conditions to be derived depend on whether the field components are the TF quantities or the SF quantities. The field components must be modified according to the requirement of the continuity across the TF–SF interface. For example, as shown in Fig. 2, the source conditions for the $\hat{E}_x$ field at the plane $k=k_0$ are given as follows:

$$\hat{E}_x^{n+l/m}\left(i+\frac{1}{2},j,k_0-1\right)=\hat{E}_x^{n+l/m}\left(i+\frac{1}{2},j,k_0-1\right)+\alpha_{z2}\times H_{y,\mathrm{inc}}^{n+l/m}\left(k_0+\frac{1}{2}\right),\tag{22}$$

$$\hat{E}_x^{n+l/m}\left(i+\frac{1}{2},j,k_0\right)=\hat{E}_x^{n+l/m}\left(i+\frac{1}{2},j,k_0\right)+\alpha_{z1}\times H_{y,\mathrm{inc}}^{n+l/m}\left(k_0-\frac{1}{2}\right)+\alpha_{z2}\times H_{y,\mathrm{inc}}^{n+l/m}\left(k_0-\frac{3}{2}\right),\tag{23}$$

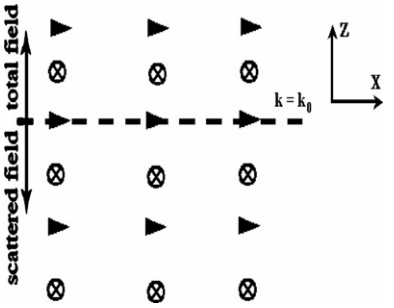

Fig. 2. The interface of TF–SF is located at the plane $k = k_0$, where the arrows denote $\hat{E}_x$, the circles denote H_y, and the dashed denotes the interface. The TF region and the SF region are located, respectively, at the top (including the interface) and at the bottom of the interface.

$$\hat{E}_x^{n+1/m}\left(i+\frac{1}{2},j,k_0+1\right)=\hat{E}_x^{n+1/m}\left(i+\frac{1}{2},j,k_0+1\right)+\alpha_{z2}\times H_{y,\mathrm{inc}}^{n+1/m}\left(k_0-\frac{1}{2}\right). \tag{24}$$

Following the similar manner, the source conditions for the other field components can be deduced.

2.5. Near-to-far-field transformation

Based on the electromagnetic equivalence principle, the NFF transformation [42,43] is an effective method to get the far-field scattering data. We use six-sided rectangular locus to enclose the structure of interest in the SF zone of the FDTD lattice, and then calculate the equivalent phasor currents using discrete Fourier transformation (DFT) applied to the computed tangential electromagnetic fields. The equation of the DFT can be defined as

$$\breve{\hat{E}}_x(f)=\sum_{n=0}^{T}\sum_{l=1}^{m}\hat{E}_x^{n+1/m}((n+\tau_l)\Delta_t)\exp(-\mathrm{j}2\pi f(n+\tau_l)\Delta_t), \tag{25}$$

where $\breve{\hat{E}}_x(f)$ is the phasor scaled electric field component, and T is the total time step equal to several wave periods at the desired frequency f.

Considering the electric and magnetic fields are interleaved in the space lattice at intervals of half space increments, we must use efficient interpolation method to obtain the values of the scattered field components at the same location. At one virtual plane $k = k_1$ on the rectangular locus, the one-dimensional fourth-order cubic interpolation formula can be defined as

$$\begin{aligned}\overline{\hat{E}}_x^{n+1/m}\left(i+\frac{1}{2},j+\frac{1}{2},k_1\right)=&\frac{-1}{16}\times\left[\hat{E}_x^{n+1/m}\left(i+\frac{1}{2},j-1,k_1\right)+\hat{E}_x^{n+1/m}\left(i+\frac{1}{2},j+2,k_1\right)\right]\\&+\frac{9}{16}\times\left[\hat{E}_x^{n+1/m}\left(i+\frac{1}{2},j,k_1\right)+\hat{E}_x^{n+1/m}\left(i+\frac{1}{2},j+1,k_1\right)\right],\end{aligned} \tag{26}$$

where $\overline{\hat{E}}_x^{n+1/m}$ is the averaged value of the scaled electric field component $\hat{E}_x^{n+1/m}$.

The two-dimensional fourth-order interpolation formula can be derived by the tensor product of the one-dimensional formulae along two orthogonal directions. As shown in Fig. 3, the weighting coefficient $W_{x,y}$ of the interpolation node is the scalar product of two weighting coefficients of the corresponding projection nodes, i.e.

$$W_{x,y}=W_xW_y,\quad x\in[i-1:i+2],\quad y\in\left[k_1-\frac{3}{2}:k_1+\frac{3}{2}\right], \tag{27}$$

where $W_{x,y}$ satisfies $\sum W_{x,y}=1$.

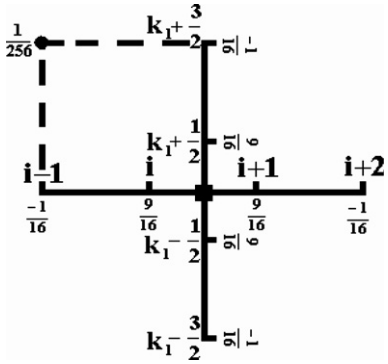

Fig. 3. The two-dimensional cubic interpolation in one cell, where the square denotes the interpolated node, and the dotted denotes one of the interpolation nodes.

Thus the two-dimensional interpolation formula can be expressed in the form

$$\begin{aligned}
&\overline{H}_x^{n+1/m}\left(i+\frac{1}{2},j+\frac{1}{2},k_1\right)\\
&=\frac{1}{256}\times\left[H_x^{n+1/m}\left(i-1,j+\frac{1}{2},k_1-\frac{3}{2}\right)+H_x^{n+1/m}\left(i+2,j+\frac{1}{2},k_1-\frac{3}{2}\right)+H_x^{n+1/m}\left(i-1,j+\frac{1}{2},k_1+\frac{3}{2}\right)\right.\\
&\left.+H_x^{n+1/m}\left(i+2,j+\frac{1}{2},k_1+\frac{3}{2}\right)\right]+\frac{-9}{256}\times\left[H_x^{n+1/m}\left(i,j+\frac{1}{2},k_1-\frac{3}{2}\right)+H_x^{n+1/m}\left(i+1,j+\frac{1}{2},k_1-\frac{3}{2}\right)\right.\\
&+H_x^{n+1/m}\left(i-1,j+\frac{1}{2},k_1-\frac{1}{2}\right)+H_x^{n+1/m}\left(i+2,j+\frac{1}{2},k_1-\frac{1}{2}\right)+H_x^{n+1/m}\left(i-1,j+\frac{1}{2},k_1+\frac{1}{2}\right)\\
&\left.+H_x^{n+1/m}\left(i+2,j+\frac{1}{2},k_1+\frac{1}{2}\right)+H_x^{n+1/m}\left(i,j+\frac{1}{2},k_1+\frac{3}{2}\right)+H_x^{n+1/m}\left(i+1,j+\frac{1}{2},k_1+\frac{3}{2}\right)\right]\\
&+\frac{81}{256}\times\left[H_x^{n+1/m}\left(i,j+\frac{1}{2},k_1-\frac{1}{2}\right)+H_x^{n+1/m}\left(i+1,j+\frac{1}{2},k_1-\frac{1}{2}\right)+H_x^{n+1/m}\left(i,j+\frac{1}{2},k_1+\frac{1}{2}\right)\right.\\
&\left.+H_x^{n+1/m}\left(i+1,j+\frac{1}{2},k_1+\frac{1}{2}\right)\right],
\end{aligned}\tag{28}$$

where $\overline{H}_x^{n+1/m}$ is the averaged value of the x component of magnetic field $\mathbf{H}^{n+1/m}$. Following Eqs. (26) and (28), the interpolation formulae for the other electromagnetic filed components can be derived.

3. Comparisons to other methods

Numerical stability and dispersion conditions for the SFDTD scheme have been analyzed in Ref. [29]. The comparisons of numerical stability and dispersion between the SFDTD scheme and the traditional FDTD method and the staggered high-order FDTD method [13,14] are presented.

The CFL number of the SFDTD scheme is 0.74312 compared with 0.57735 for the traditional FDTD method. The high-order FDTD method, which is second-order accurate in time and fourth-order accurate in space, is referred to as FDTD(2,4). The CFL number of the FDTD(2,4) method is 0.49487, lower than that of the SFDTD scheme.

Using the uniform space increment and stability criterion $\mathrm{CFL}_\delta = 0.5$, Fig. 4 shows relative phase velocity error as a function of points per wavelength (PPW) for a plane wave traveling at $\theta = 0^\circ$ and $\phi = 45^\circ$. What is more, Fig. 5 shows the relative error at $\phi = 0^\circ$ versus the propagating angle θ with the PPW=10. Next we change the point numbers to be 8, 10, and 12 in the x, y, and z directions, reset the CFL number to be $\mathrm{CFL}_x = 0.4$, $\mathrm{CFL}_y = 0.5$, and $\mathrm{CFL}_z = 0.6$, then redraw the relative error at $\theta = 45^\circ$ versus the propagating angle ϕ in Fig. 6.

According to Figs. 4–6, the SFDTD scheme has less dispersion than both the traditional FDTD method and the FDTD(2,4) method. Accordingly, the SFDTD scheme allows coarser grids within a given error bound, which in turn results in shorter CPU time and less storage.

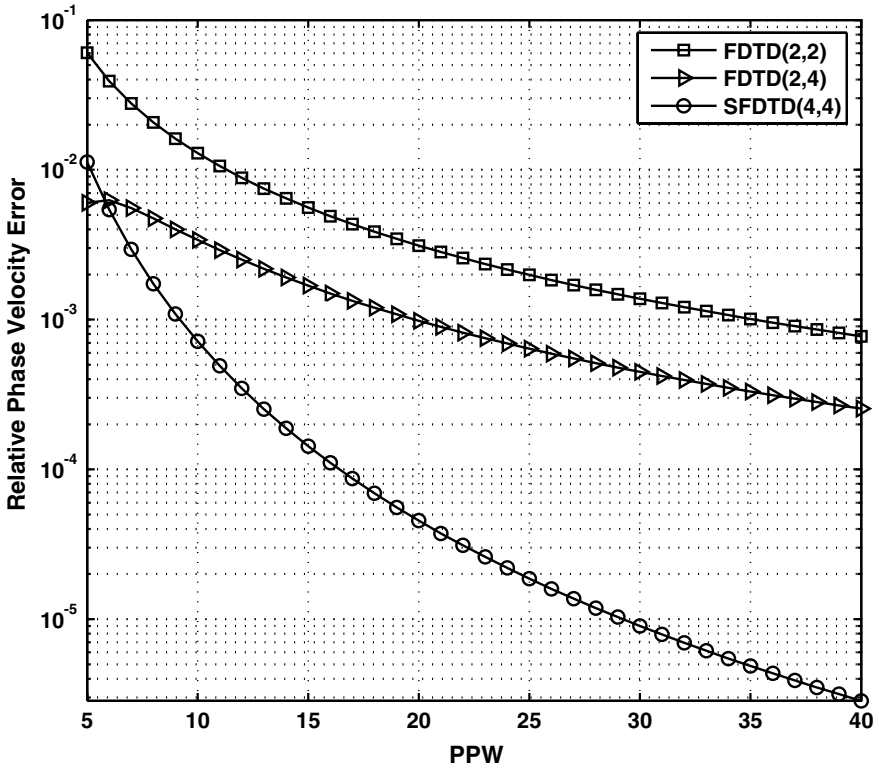

Fig. 4. Dispersion curves for a plane wave traveling at $\theta = 0^\circ$ and $\phi = 45^\circ$ versus points per wavelength (PPW) discretization: $\mathrm{CFL}_\delta = 0.5$.

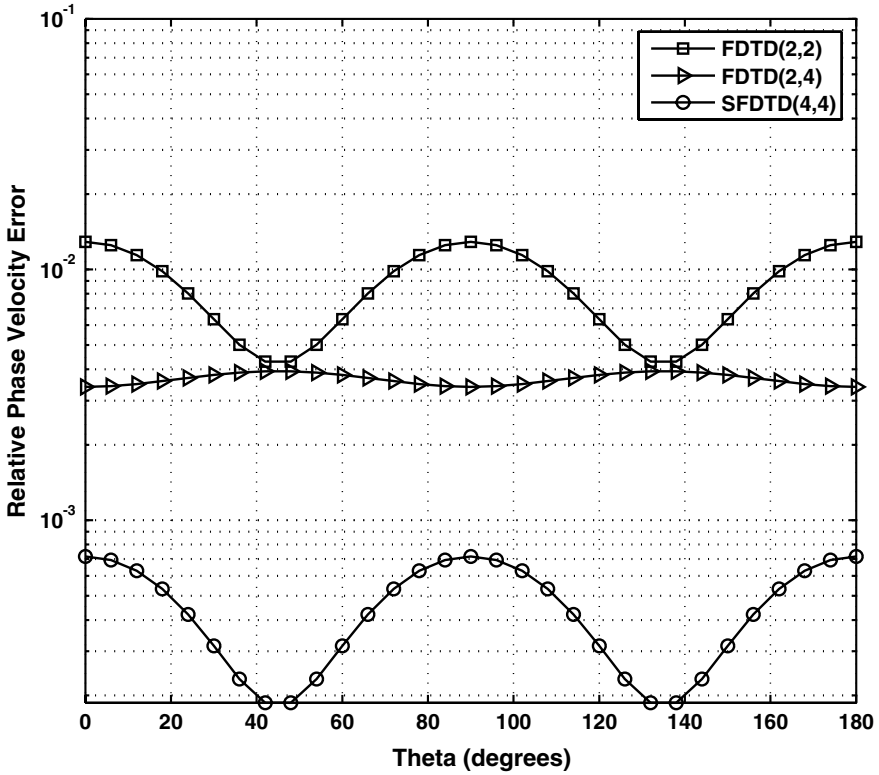

Fig. 5. Dispersion curves for a plane wave traveling at $\phi = 0^\circ$ versus the propagating angle θ: PPW = 10 and $\mathrm{CFL}_\delta = 0.5$.

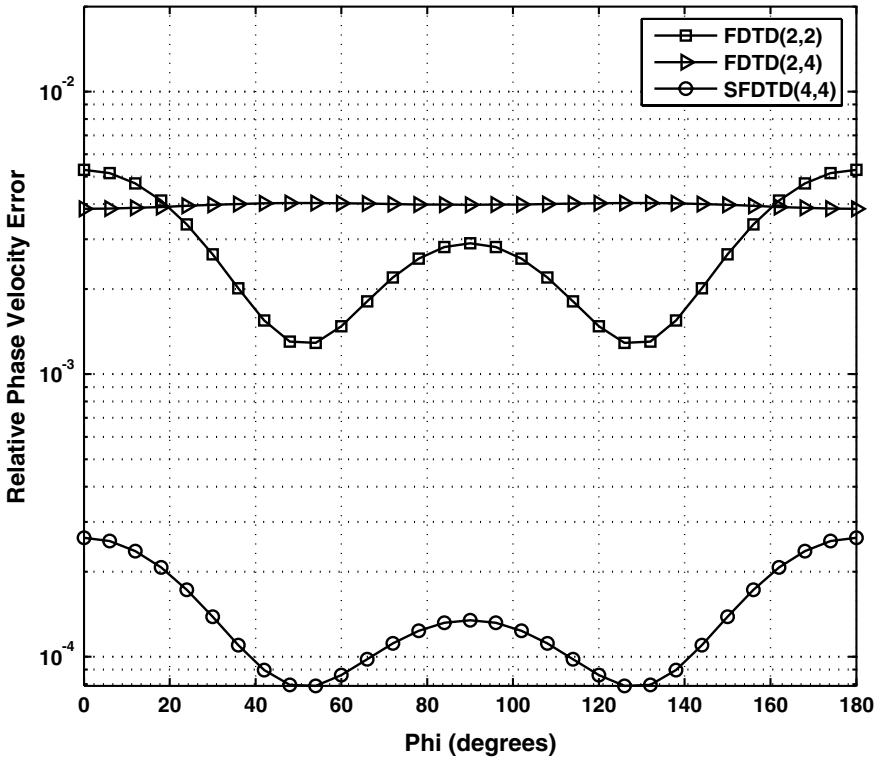

Fig. 6. Dispersion curves for a plane wave traveling at $\theta = 45^\circ$ versus the propagating angle ϕ: point numbers in x, y, and z directions are, respectively, 8, 10, and 12, $\mathrm{CFL}_x = 0.4$, $\mathrm{CFL}_y = 0.5$, and $\mathrm{CFL}_z = 0.6$.

The symplectic integrator is superior to the fourth-order-accurate R–K method [44] in the temporal direction. Firstly, in view of the amplification factor, the symplectic scheme is nondissipative, but the four-stage R–K method is dissipative. Hence the R–K method produces amplitude error. Secondly, the R–K method requires additional memory in contrast with the SDTD scheme.

In 1989, Fang proposed another high-order-accurate FDTD method referred to as FDTD(4,4) method [45], which is fourth-order accurate in both space and time. Compared with the FDTD(4,4) method using third-order spatial derivatives to substitute for third-order correctional temporal derivatives, the SFDTD scheme using the simple air–dielectric treatment is easier to treat the varying of permittivity and permeability in the inhomogeneous domain.

4. Numerical results

4.1. One-dimensional propagation problems

The one-dimensional hard source can be given by

$$\hat{E}_{x,\mathrm{inc}}^{n+l/m}(k_s) = \sqrt{\varepsilon_0/\mu_0}\exp\left[-\frac{1}{2}\times\left(\frac{(n+\tau_l)-40}{10}\right)^2\right]. \tag{29}$$

Long-term simulation is implemented with $\mathrm{CFL}_z = 0.48$, $\Delta_z = 1$ cm, and $T = 3000$. By using the perfect electric conductor (PEC) boundary, the one-dimensional resonant cavity is constructed. In Fig. 7a, the nonphysical oscillation is introduced into the solution of the traditional FDTD method and the FDTD(2,4) method. Contrarily, the SFDTD scheme keeps stable and accurate.

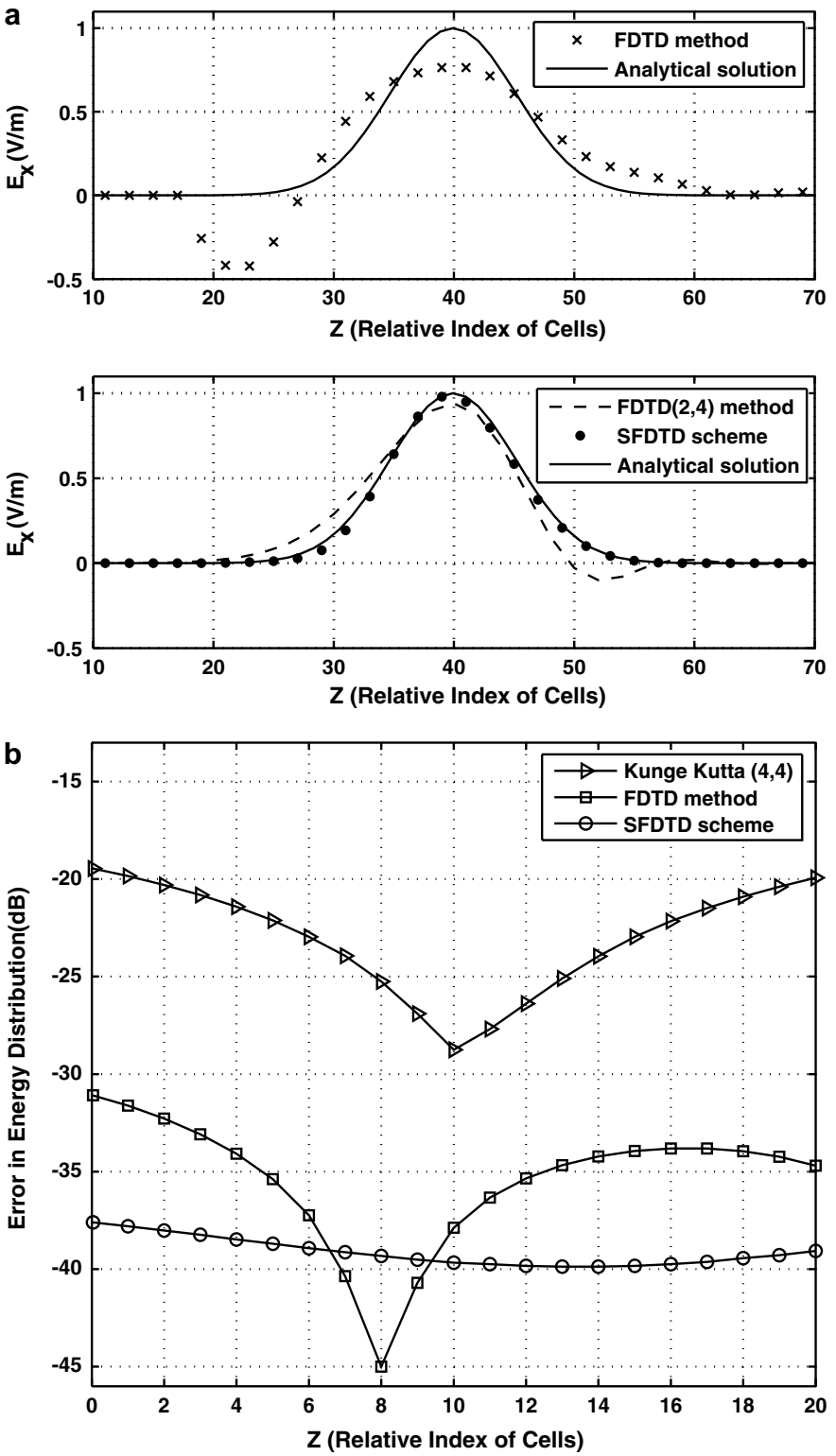

Fig. 7. The propagation of the one-dimensional Gaussian pulse: $\Delta_z = 1$ cm, $\mathrm{CFL}_z = 0.48$, and $T = 3000$. (a) The time-domain waveforms, PEC boundary. (b) The error in energy distribution, ABC boundary.

To verify the energy-conserving characteristic hold for the symplectic scheme, the error in energy distribution defined by $\eta = 10\log_{10}\left|\frac{1}{2}|\breve{\hat{E}}_{x,\mathrm{inc}}(f)/\breve{\Psi}(f)|^2 + \frac{1}{2}|\breve{H}_{y,\mathrm{inc}}(f)/\breve{\Psi}(f)|^2 - 1\right|$ is illustrated in Fig. 7b. Here the PML ABC is employed. In view of the smaller fluctuation and lower error, the SFDTD scheme better preserves the symplectic structure of the electromagnetic system. But the explicit R–K method, which is explicit fourth-order accurate in both space and time, is dissipative. Hence, as the time step increases, the energy of the electromagnetic system computed by the R–K method is gradually attenuated.

4.2. Three-dimensional radiation problems

The electric pole as soft source is implemented by (30) using the uniform space increment Δ_δ.

$$\hat{E}_x^{n+l/m}(k_\mathrm{s}) = \hat{E}_x^{n+l/m}(k_\mathrm{s}) - 2\times 10^{-10} d_l \times \mathrm{CFL}_\delta \times \exp\left[-\left(\frac{(n+\tau_l)\Delta_t}{\tau_0} - 3\right)^2\right] \frac{[(n+\tau_l)\Delta_t - 3\tau_0]}{\tau_0^2 \Delta_\delta^2}, \tag{30}$$

where $\tau_0 = 2\times 10^{-9}$ s.

We consider a computational domain of $24\times 24\times 24$ cells of vacuum, surrounded by 10-cell PML layers. The vertical dipole is located near the center of the domain at the source point k_s $(12+\frac{1}{2}, 12, 12)$, and the recorded E_x field is located 2 cells from the absorbing boundary of the computational domain at point $(12+\frac{1}{2}, 12, 22)$. With the space increment $\Delta_\delta = 10$ cm and the CFL number $\mathrm{CFL}_\delta = 0.5$, the waveforms of the E_x field within 20 ns are given in Fig. 8. The SFDTD scheme reduces 70% of global L_2 error compared to the traditional FDTD method.

The point k_s and the absorbing boundary are relocated, respectively, 2 m and 0.2 m form the recorded E_x field, and the simulation time is chosen to be 30 ns. The traditional FDTD method occupies $108\times 108\times 108$ cells with $\Delta_\delta = 5$ cm and $\mathrm{CFL}_\delta = 0.5$, by contrast, the SFDTD scheme occupies $66\times 66\times 66$ cells with $\Delta_\delta = 10$ cm and

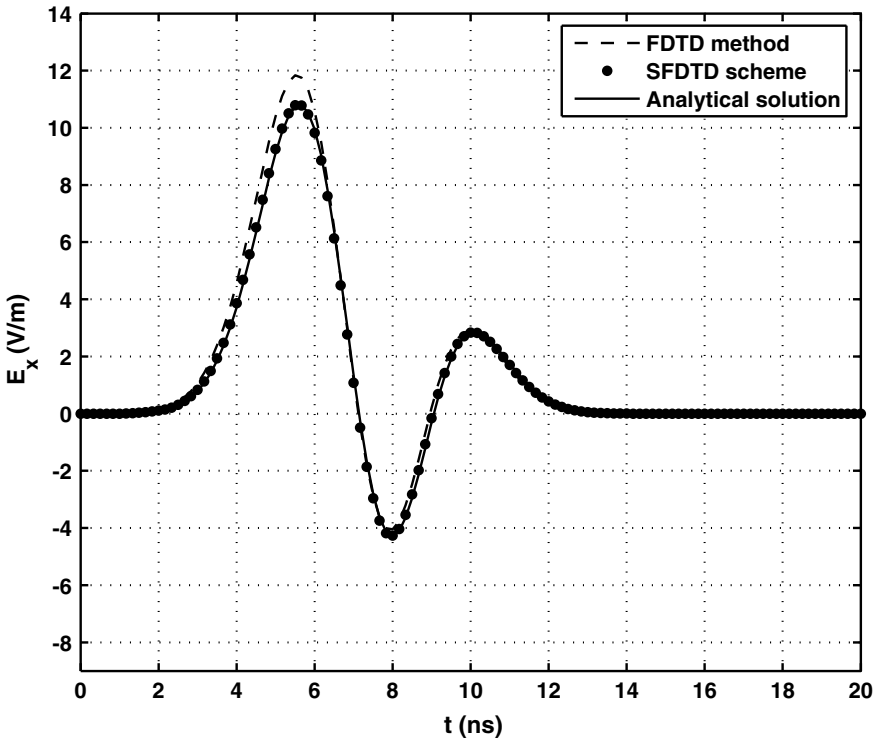

Fig. 8. The radiation field of the vertical electric dipole: $\Delta_\delta = 10$ cm and $\mathrm{CFL}_\delta = 0.5$.

Table 1
The comparisons of computational statistics with the same global L_2 error

	Memory (MB)	Time (s)
FDTD	173	382
SFDTD	50	96

For the traditional FDTD method, $108 \times 108 \times 108$ cells, $\Delta_\delta = 5$ cm, and $\mathrm{CFL}_\delta = 0.5$, by contrast, for the SFDTD scheme, $66 \times 66 \times 66$ cells, $\Delta_\delta = 10$ cm, and $\mathrm{CFL}_\delta = 0.6$.

$\mathrm{CFL}_\delta = 0.6$. The comparisons of the memory and the CPU time are listed in Table 1. Under the same global L_2 error condition, about 70% of computational resources are saved by the SFDTD scheme.

4.3. Three-dimensional scattering problems

4.3.1. Perfectly conducting cube

Here we consider the scattering of a plane wave incident on a perfectly conducting cube with the side length of 1 m. The settings are taken as $\Delta_x = 0.5/6$ m, $\Delta_y = 0.5/5$ m, $\Delta_z = 0.5/7$ m, $\mathrm{CFL}_x = 0.5736$, $\mathrm{CFL}_y = 0.4780$, $\mathrm{CFL}_z = 0.6692$, and $T = 380$. The total domain occupies $55 \times 54 \times 57$ cells, and the PML layers are spanned by 10 cells. The solution of the traditional FDTD method disagrees with the solution of moment methods over the frequency range from 200 MHz to 300 MHz. However, the solution of the SFDTD scheme is accurate because of the stable time evolution of the Hamiltonian (see Fig. 9).

4.3.2. Lossy dielectric sphere

The example considered is a lossy dielectric sphere with the relative permittivity of 30, the conductivity of 0.3, and the radius of 10 cm. The z-axial electric field component is calculated by the SFDTD scheme through the DFT equation. The parameter values are fixed as follows: $\mathrm{CFL}_\delta = 0.7$, $\Delta_\delta = 2$ cm, and $f = 200$ MHz. The solution of the Mie series is given as reference solution. Fig. 10 compares the averaged material solution and the local material solution. The result obtained by the averaged material strategy given in (17) agrees with the Mie series solution very well, but the local material solution leads to the presence of peaks at the air–dielectric interface.

We reset the CFL number to be $\mathrm{CFL}_\delta = 0.5$, then repeatedly compute the $\breve{\hat{E}}_x(f)$ field within the lossy sphere along the z-axis with coordinates $x = \Delta_\delta/2$ and $y = 0$. The uniform space increments are taken as 2.0 cm, 1.0 cm, and 0.5 cm. The FDTD and the SFDTD solutions using the local material (LM), the staircased model (SM), and the averaged material (AM) are given for comparison. Different from the LM strategy, the material settings for the SM do not depend on the original positions of the electric field components but the approximate positions by the staircasing approach. We use two error criterions to evaluate various methods, which are global relative L_2 error and maximal local relative error. As the numerical fault increases, we give the rank from 1 to 6 for these methods. As indicated in Table 2, we can come to a conclusion as follows:

(i) The smaller space increment we fix, the higher numerical precision we get, no matter what methods we adopt.
(ii) For both the FDTD method and the SFDTD scheme, the SM strategy obtains lower global error but higher local error due to the staircase approximation for the curved boundaries. Contrarily, the LM strategy presents its advantage over the SM strategy for reducing the local error.
(iii) Whatever criterions we apply, the SFDTD scheme using the AM achieves the most accurate results in all the methods. At least 75% of error is reduced by the averaged SFDTD scheme compared with the averaged FDTD method and those non-averaged SFDTD schemes.

Based on the above analysis and numerical results in Table 2, the proposed strategy is efficient for treating the heterogeneous geometries.

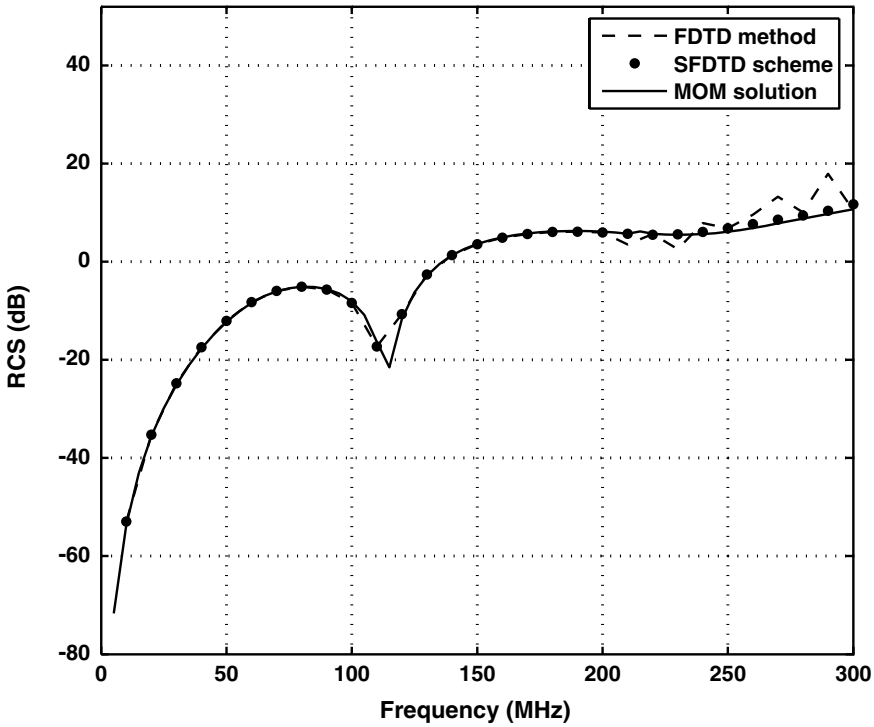

Fig. 9. The monostatic RCS of the perfectly conducting cube: $\Delta_x = 0.5/6$ m, $\Delta_y = 0.5/5$ m, $\Delta_z = 0.5/7$ m, $\mathrm{CFL}_x = 0.5736$, $\mathrm{CFL}_y = 0.4780$, $\mathrm{CFL}_z = 0.6692$, and $T = 380$.

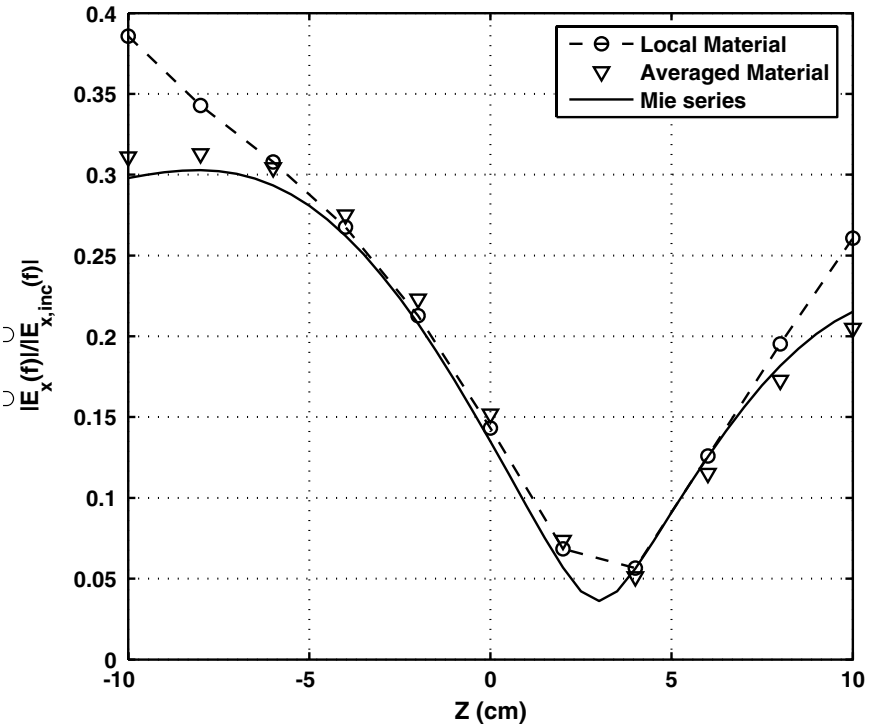

Fig. 10. The z-axial electric field of the lossy dielectric sphere: $\Delta_\delta = 2$ cm, $\mathrm{CFL}_\delta = 0.7$, and $f = 200$ MHz.

Table 2
The comparisons of the FDTD method and the SFDTD scheme using the local material (LM), the staircased model (SM), and the averaged material (AM)

Method	Δ_δ (cm)	Err_{L_2}	Rank	$\mathrm{Err}_{\mathrm{Max}}$	Rank
FDTD (LM)	2.0	8.04×10^{-2}		1.82×10^{-1}	
FDTD (LM)	1.0	3.59×10^{-2}	5	9.55×10^{-2}	2
FDTD (LM)	0.5	2.17×10^{-2}		6.40×10^{-2}	
FDTD (SM)	2.0	5.77×10^{-2}		3.38×10^{-1}	
FDTD (SM)	1.0	2.96×10^{-2}	3	2.54×10^{-1}	6
FDTD (SM)	0.5	1.66×10^{-2}		1.14×10^{-1}	
FDTD (AM)	2.0	7.24×10^{-2}		3.16×10^{-1}	
FDTD (AM)	1.0	3.64×10^{-2}	4	1.14×10^{-1}	4
FDTD (AM)	0.5	1.77×10^{-2}		1.03×10^{-1}	
SFDTD (LM)	2.0	8.21×10^{-2}		2.11×10^{-1}	
SFDTD (LM)	1.0	3.76×10^{-2}	6	1.05×10^{-1}	3
SFDTD (LM)	0.5	2.26×10^{-2}		6.80×10^{-2}	
SFDTD (SM)	2.0	5.60×10^{-2}		3.05×10^{-1}	
SFDTD (SM)	1.0	2.88×10^{-2}	2	2.50×10^{-1}	5
SFDTD (SM)	0.5	1.62×10^{-2}		1.15×10^{-1}	
SFDTD (AM)	2.0	1.38×10^{-2}		4.49×10^{-2}	
SFDTD (AM)	1.0	7.17×10^{-3}	1	2.49×10^{-2}	1
SFDTD (AM)	0.5	2.85×10^{-3}		1.42×10^{-2}	

The global relative L_2 error (Err_{L_2}) and the maximal local relative error ($\mathrm{Err}_{\mathrm{Max}}$) are adopted. The lower rank denotes the higher numerical precision. The uniform space increments are taken as 2.0 cm, 1.0 cm, and 0.5 cm, and the CFL number is chosen to be 0.50.

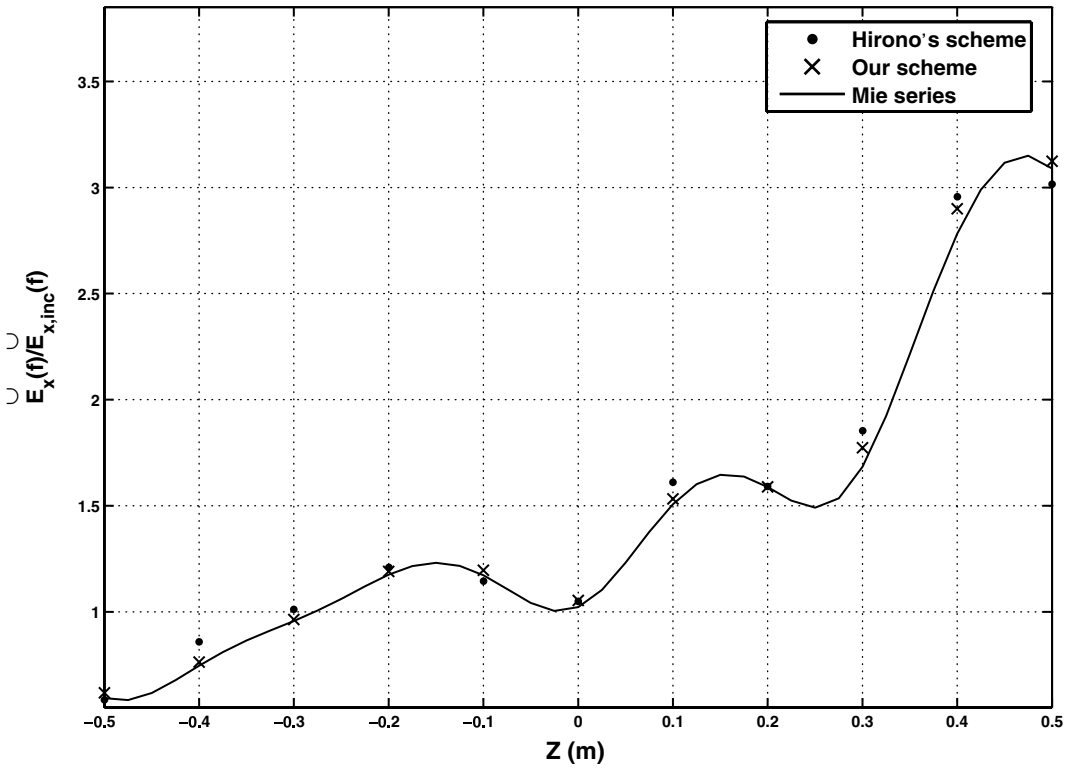

Fig. 11. The z-axial electric field of the lossless dielectric sphere: $\Delta_\delta = 0.1$ m, $\mathrm{CFL}_\delta = 0.5$, and $f = 400$ MHz. The global relative L_2 error for Hirono's scheme and our scheme are, respectively, 0.0552 and 0.0295. The maximal local relative error for Hirono's scheme and our scheme are, respectively, 0.1508 and 0.0534.

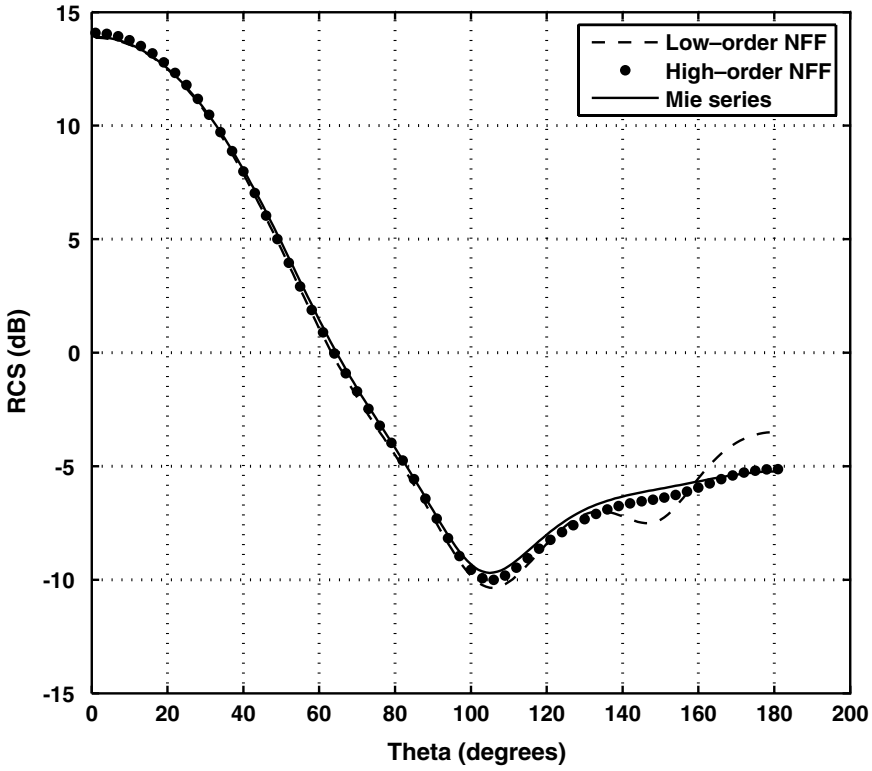

Fig. 12. The E-plane bistatic RCS of the lossless dielectric sphere: $\Delta_\delta = 0.1$ m and $\mathrm{CFL}_\delta = 0.5$.

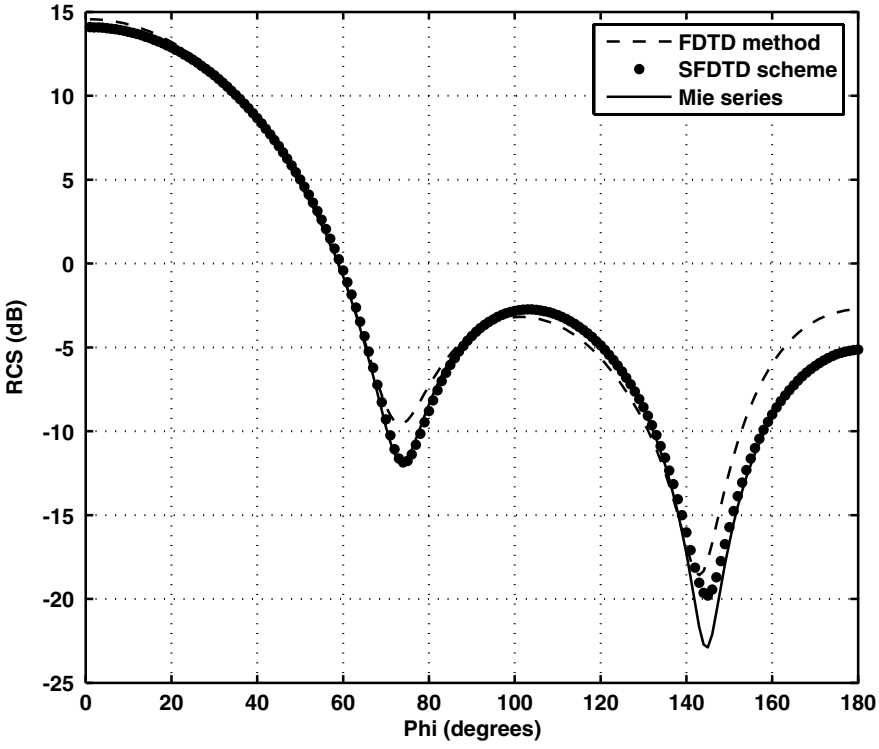

Fig. 13. The H-plane bistatic RCS of the lossless dielectric sphere: $\Delta_\delta = 0.1$ m and $\mathrm{CFL}_\delta = 0.5$.

4.3.3. Lossless dielectric sphere

The scattering of a plane wave by a lossless dielectric sphere of the relative permittivity $\varepsilon_r = 2$ is analyzed. The wavelength of the incident wave is 1 m, the radius of the sphere is 0.5 m, the uniform space increment is $\Delta_\delta = 0.1$ m, and the CFL number is $\mathrm{CFL}_\delta = 0.5$.

The z-axial electric field of the lossless dielectric sphere is computed by using different material interface treatments. According to Fig. 11, our scheme is superior to Hirono's scheme.

In conjunction with the low-order and the high-order NFF transformation, the SFDTD scheme is used to calculate the bistatic E-plane RCS of the dielectric sphere. It can be seen from Fig. 12, the high-order NFF transformation represents better accuracy at the scattering angle from 130° to 180°.

The bistatic H-plane RCS is displayed in Fig. 13. From the figure, it can be inferred that even if using coarser grids, the SFDTD scheme can still acquire high-order accuracy.

5. Conclusion

The SFDTD scheme, which is explicit fourth-order accurate in both space and time, is accurate, energy-conserving, highly stable, and efficient. On the one hand, the scheme can achieve high-order accuracy by using the fourth-order spatial difference with the simple Yee lattice. On the other hand, by using the symplectic integrator, the scheme demonstrates desirable numerical performance under long-term simulation. Finally, with the aid of the air–dielectric interface treatment and the high-order NFF transformation, the accuracy of the scheme for the near-field and the far-field response is maintained. In short, the SFDTD scheme can save computational resources by using coarse grids or high CFL number.

The main disadvantage of the scheme is that it requires at least four stages for fourth-order accuracy and hence four times the work. Fortunately, this can be offset by using coarser grids or improved by constructing the optimum symplectic integrator.

Acknowledgments

This work was supported by the National Natural Science Foundation of China (No. 60371041 and No. 60671051). The authors thank the referees and the associate editor for their invaluable comments and suggestions.

References

[1] A. Taflove, Computational Electrodynamics: The Finite-Difference Time-Domain Method, Artech House, Norwood, MA, 1995.
[2] D.M. Sullivan, Electromagnetic Simulation Using the FDTD Method, IEEE Press, New York, 2000.
[3] V. Shankar, A.H. Mohammadian, W.F. Hall, A time-domain, finite-volume treatment for the Maxwell equations, Electromagnetics 10 (1990) 127–145.
[4] C.D. Munz, P. Ommes, R. Schneider, A three-dimensional finite-volume solver for the Maxwell equations with divergence cleaning on unstructured meshes, Computer Physics Communications 130 (2000) 83–117.
[5] S. Piperno, M. Remaki, L. Fezoui, A nondiffusive finite volume scheme for the three-dimensional Maxwell's equations on unstructured meshes, SIAM Journal on Numerical Analysis 39 (2002) 2089–2108.
[6] J.F. Lee, R. Lee, A. Cangellaris, Time-domain finite-element methods, IEEE Transactions on Antennas and Propagation 45 (1997) 430–442.
[7] G. Rodrigue, D. White, A vector finite element time-domain method for solving Maxwell's equations on unstructured hexahedral grids, SIAM Journal on Scientific Computing 23 (2001) 683–706.
[8] D. Jiao, J.M. Jin, Three-dimensional orthogonal vector basis functions for time-domain finite element solution of vector wave equations, IEEE Transactions on Antennas and Propagation 51 (2003) 59–66.
[9] J.S. Hesthaven, T. Warburton, Nodal high-order methods on unstructured grids – I. Time-domain solution of Maxwell's equations, Journal of Computational Physics 181 (2002) 186–221.
[10] T. Lu, W. Cai, P.W. Zhang, Discontinuous Galerkin time-domain method for GPR simulation in dispersive media, IEEE Transactions on Geoscience and Remote Sensing 43 (2005) 72–80.
[11] M. Bernacki, S. Lanteri, S. Piperno, Time-domain parallel simulation of heterogeneous wave propagation on unstructured grids using explicit, nondiffusive, discontinuous Galerkin methods, Journal of Computational Acoustics 14 (2006) 57–81.
[12] M. Krumpholz, L.P.B. Katehi, MRTD: new time-domain schemes based on multiresolution analysis, IEEE Transactions on Microwave Theory and Techniques 44 (1996) 555–571.

[13] S.V. Georgakopoulos, C.R. Birtcher, C.A. Balanis, R.A. Renaut, Higher-order finite-difference schemes for electromagnetic radiation, scattering, and penetration, Part I: Theory, IEEE Antennas and Propagation Magazine 44 (2002) 134–142.
[14] S.V. Georgakopoulos, C.R. Birtcher, C.A. Balanis, R.A. Renaut, Higher-order finite-difference schemes for electromagnetic radiation, scattering, and penetration, Part 2: Applications, IEEE Antennas and Propagation Magazine 44 (2002) 92–101.
[15] J.M. Sanz-Serna, M.P. Calvo, Numerical Hamiltonian Problems, Chapman & Hall, London, UK, 1994.
[16] H. Yoshida, Construction of higher order symplectic integrators, Physica D: Nonlinear Phenomena 46 (1990) 262.
[17] M. Suzuki, General theory of higher-order decomposition of exponential operators and symplectic integrators, Physics Letters A 165 (1992) 387–395.
[18] L. Jay, Symplectic partitioned Runge–Kutta methods for constrained hamiltonian systems, SIAM Journal on Numerical Analysis 33 (1996) 368.
[19] M. Sofroniou, W. Oevel, Symplectic Runge–Kutta schemes I: order conditions, SIAM Journal on Numerical Analysis 34 (1997) 2063–2086.
[20] S.A. Chin, Symplectic integrators from composite operator factorizations, Physics Letters A 226 (1997) 344–348.
[21] T. Hirono, W.W. Lui, K. Yokoyama, Time-domain simulation of electromagnetic field using a symplectic integrator, IEEE Microwave and Guided Wave Letters 7 (1997) 279–281.
[22] T. Hirono, W.W. Lui, K. Yokoyama, S. Seki, Stability and numerical dispersion of symplectic fourth-order time-domain schemes for optical field simulation, Journal of Lightwave Technology 16 (1998) 1915–1920.
[23] H. Zhi-Xiang, W. Xian-Liang, A second-order symplectic partitioned Runge–Kutta scheme for Maxwell's equations, Applied Computational Electromagnetics Society Journal 20 (2005) 235–239.
[24] S. Reich, Multi-symplectic Runge–Kutta collocation methods for Hamiltonian wave equations, Journal of Computational Physics 157 (2000) 473–499.
[25] T.J. Bridges, S. Reich, Multi-symplectic integrators: numerical schemes for Hamiltonian PDEs that conserve symplecticity, Physics Letters A 284 (2001) 184–193.
[26] H.Y. Liu, K. Zhang, Multi-symplectic Runge–Kutta-type methods for Hamiltonian wave equations, IMA Journal of Numerical Analysis 26 (2006) 252–271.
[27] L. Qinghong, S. Yongzhong, W. Yushun, On multi-symplectic partitioned Runge–Kutta methods for Hamiltonian wave equations, Applied Mathematics and Computation 177 (2006) 36–43.
[28] I. Saitoh, Y. Suzuki, N. Takahashi, The symplectic finite difference time domain method, IEEE Transactions on Magnetics 37 (2001) 3251–3254.
[29] T. Hirono, W. Lui, S. Seki, Y. Yoshikuni, A three-dimensional fourth-order finite-difference time domain scheme using a symplectic integrator propagator, IEEE Transactions on Microwave Theory and Techniques 49 (2001) 1640–1648.
[30] M. Kusaf, A.Y. Oztoprak, D.S. Daoud, Optimized exponential operator coefficients for symplectic FDTD method, IEEE Microwave and Wireless Components Letters 15 (2005) 86–88.
[31] P.W. Zhai, G.W. Kattawar, P. Yang, C.H. Li, Application of the symplectic finite-difference time-domain method to light scattering by small particles, Applied Optics 44 (2005) 1650–1656.
[32] W. Sha, Z.X. Huang, X.L. Wu, M.S. Chen, Total field and scattered field technique for fourth-order symplectic finite difference time domain method, Chinese Physics Letters 23 (2006) 103–105.
[33] N. Anderson, A.M. Arthurs, Helicity and variational principles for Maxwell's equations, International Journal of Electronics 54 (1983) 861–864.
[34] J.L. Young, D. Gaitonde, J.J.S. Shang, Toward the construction of a fourth-order difference scheme for transient EM wave simulation: staggered grid approach, IEEE Transactions on Antennas and Propagation 45 (1997) 1573–1580.
[35] J.S. Shang, High-order compact-difference schemes for time-dependent Maxwell equations, Journal of Computational Physics 153 (1999) 312–333.
[36] A. Yefet, P.G. Petropoulos, A staggered fourth-order accurate explicit finite difference scheme for the time-domain Maxwell's equations, Journal of Computational Physics 168 (2001) 286–315.
[37] Z.Q. Xie, C.H. Chan, B. Zhang, An explicit fourth-order staggered finite-difference time-domain method for Maxwell's equations, Journal of Computational and Applied Mathematics 147 (2002) 75–98.
[38] S. Zhao, G.W. Wei, High-order FDTD methods via derivative matching for Maxwell's equations with material interfaces, Journal of Computational Physics 200 (2004) 60–103.
[39] J.P. Berenger, A perfectly matched layer for the absorption of electromagnetic-waves, Journal of Computational Physics 114 (1994) 185–200.
[40] J.P. Berenger, Three-dimensional perfectly matched layer for the absorption of electromagnetic waves, Journal of Computational Physics 127 (1996) 363–379.
[41] T. Hirono, W.W. Lui, S. Seki, Successful applications of PML-ABC to the symplectic FDTD scheme with 4th-order accuracy in time and space, IEEE MTT-S International Microwave Symposium Digest 3 (1999) 1293–1296.
[42] A. Taflove, Application of the finite-difference time-domain method to sinusoidal steady-state electromagnetic-penetration problems, IEEE Transactions on Electromagnetic Compatibility EMC-22 (1980) 191–202.
[43] K. Umashankar, A. Taflove, Novel method to analyze electromagnetic scattering of complex objects, IEEE Transactions on Electromagnetic Compatibility EMC-24 (1982) 397–405.
[44] A. Taflove et al., Advances in Computational Electrodynamics: The Finite-Difference Time-Domain Method, Artech House, Norwood, MA, 1998.
[45] J. Fang, Time Domain Finite Difference Computation for Maxwell's Equations, Dept. Elect. Eng., Univ. California, Berkeley, CA, 1989.